Machine Learning to Predict Quasi TE_{011} Mode Resonances in Double-Stacked Dielectric Cavities

Charles Lewis, *Graduate Student Member, IEEE*, Jordan Bryan, Nathan Schwartz, Jonathan Hale, Kane Fanning, and John S. Colton

***Abstract*— We have applied machine learning in a neural network to calculate the quasi TE_{011} mode of a cylindrical microwave cavity with two symmetrically stacked dielectric resonators (DRs) inside, with aspect ratios of the overall cavity being limited to the range of 0.25–4. The neural network was trained with 99 970 samples and evaluated using 9564 samples from a holdout dataset. The samples were created using a supercomputer to solve random cavity configurations via finite-element method (FEM) programming. The trained neural network predicts the resonant frequency of the quasi TE_{011} mode and expresses the mode in terms of expansion coefficients of empty cavity TE_{0np} modes, from which plots of the electric and magnetic fields can be made. The predictions are extremely quick, taking ∼0.05–0.2 s running on a typical personal computer, and are very accurate when judged against the FEM results: the overall median error in the frequency neural network is 0.2%, and the overall median error of the expansion coefficients neural network is 0.003%. This should allow designers to much more rapidly determine optimal cavity and DR dimensions and other parameters in order to achieve the frequency and mode they desire, with a speedup of approximately 10 000× compared with FEM calculations alone. A link to the Python implementation of our FEM code and our trained neural network code is provided.**

***Index Terms*— Cavity resonators, dielectric resonators (DRs), electromagnetic fields, machine learning, neural networks.**

I. Introduction

RESONANT microwave cavities, namely, hollow metal cavities in which microwaves can form standing wave patterns in the electric and magnetic fields, have been studied and used for decades. A sampling of applications includes concentrating fields for electron spin resonance (ESR) [1]–[4], microwave cavity resonance spectroscopy (MCRS) for studying plasmas [5], to enhance particle accelerators [6], measuring dielectric constants of materials [7], [8], microwave filters [9]–[11], and antennae [12]–[15]. Such cavities typically are characterized by high quality factors (Q-factors) and sharp resonances at specific frequencies.

Although there are an infinite number of cavity modes, one of the most important for an empty cylindrical cavity is the TE_{011} mode. The three mode numbers $(m, n, p) = (0, 1, 1)$ indicate no azimuthal ϕ dependence, a single antinode in the radial r-direction, and a single antinode in the longitudinal z-direction, respectively. The topology of the mode is described by having an electric field only in the ϕ-direction and having a magnetic field only in the r- and z-directions. The electric field has a node along the axis of the cylinder, whereas there is a strong on-axis magnetic field B_z. The TE_{011} mode of two representative cavities is plotted in Fig. 1(a) and (c). From an ESR point of view, the center of the cavity provides a desirable spot for a sample, with a large magnetic field and small electric field, and the surface currents allow holes to be made in the side of the cavity for optical access without substantial degradation of the cavity quality [16].

When the cavity is not empty, the fields change compared with the fields in a pure TE_{011} mode. However, there will typically still be a single mode with the same topology as the TE_{011} mode of an empty cavity: **E** being only in the ϕ-direction, **B** being only in r- and z-directions, and a large B-field/small E-field at the center. This is termed the "quasi TE_{011}" mode. The quasi TE_{011} modes for two representative nonempty cavities are plotted in Fig. 1(b) and (d), with these cavities containing two symmetrically placed vertically stacked pieces of high dielectric material, so-called "dielectric resonators" (DRs).

DRs have been used with and without surrounding metal cavities for decades as a vehicle for concentrating the fields, typically at microwave frequencies; as the article by Richtmyer [17] in 1939 declared, "suitably shaped objects made of a dielectric material can function as electrical resonators for high frequency oscillations." As noted above, one of the main applications of microwave cavities has been ESR; and one of the main applications of the enhanced field provided by DRs has been to enhance the ESR signal. This was first observed by Carter and Okaya [18] in 1960, who used pieces of Fe-doped rutile as the DRs. Other ESR articles employing DRs have followed through the decades since, consistently pointing out the ability of DRs to enhance the

Manuscript received October 25, 2021; revised December 30, 2021; accepted January 18, 2022. Date of publication February 10, 2022; date of current version April 4, 2022. This work was supported in part by Brigham Young University (BYU) College of Physical and Mathematical Sciences and in part by the Department of Physics and Astronomy. *(Corresponding author: John S. Colton.)*

Charles Lewis is with the Department of Physics, University of Washington, Seattle, WA 98195 USA (e-mail: charles.lewis217@gmail.com).

Jordan Bryan was with the Department of Physics, Illinois State University, Normal, IL 61790 USA (e-mail: jnbrya1@ilstu.edu).

Nathan Schwartz was with the Department of Physics and Astronomy, Brigham Young University, Provo, UT 84602 USA. He is now with the Core Consulting Group, Oliver Wyman, Dallas, TX 75201 USA (e-mail: nate.r.schwartz@gmail.com).

Jonathan Hale is with the Department of Mathematics, Brigham Young University, Provo, UT 84602 USA (e-mail: jonathan.h.hale98@gmail.com).

Kane Fanning is with the Department of Physics and Astronomy, Brigham Young University, Provo, UT 84602 USA (e-mail: kanefanning@gmail.com).

John S. Colton is with the Department of Physics and Astronomy, Brigham Young University, Provo, UT 84602 USA (e-mail: john_colton@byu.edu).

This article has supplementary material provided by the authors and color versions of one or more figures available at https://doi.org/10.1109/TMTT.2022.3145357.

Digital Object Identifier 10.1109/TMTT.2022.3145357

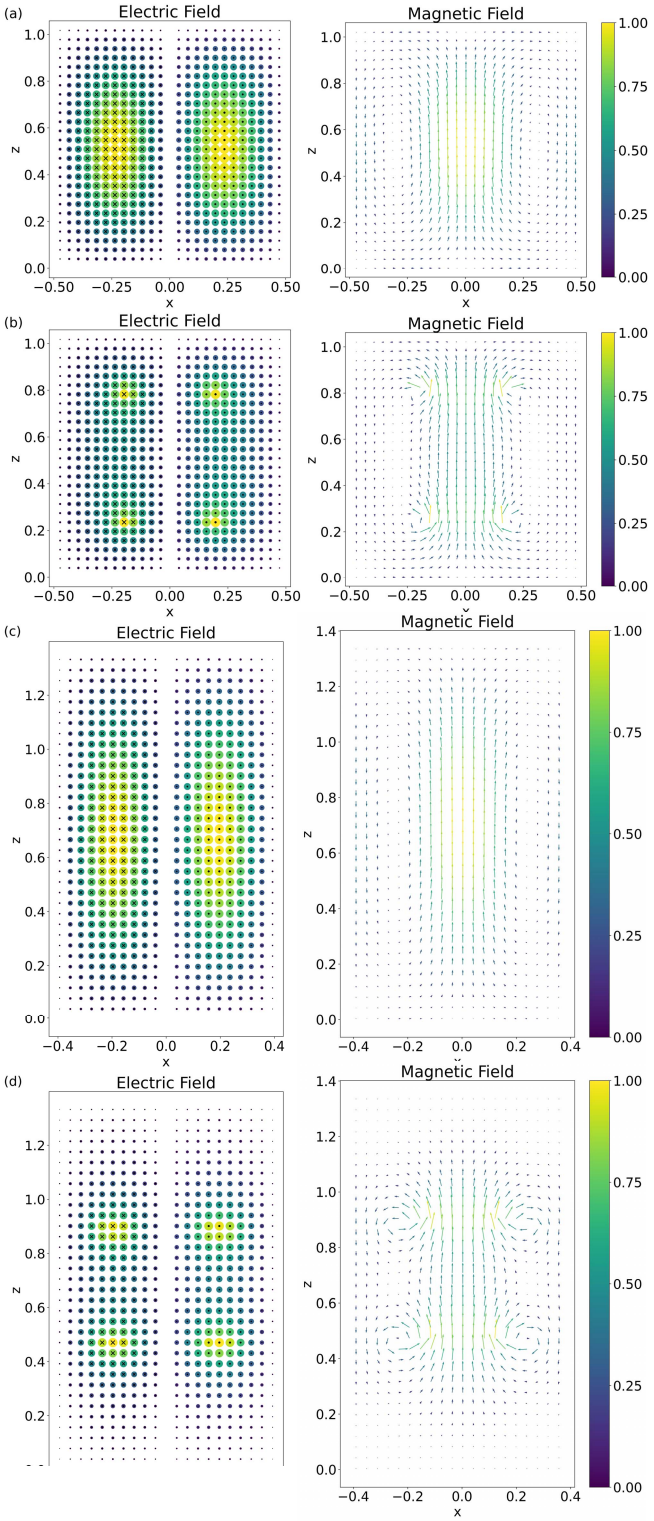

Fig. 1. Cavity modes of electric and magnetic fields plotted in cross section; the magnetic fields being calculated through Faraday's law and the curl of the electric field. The cavities use normalized dimensions such that HM as defined by (5) equals unity. (a) TE_{011} mode of an empty cylindrical cavity and (b) quasi TE_{011} mode of the same cavity but with double-stacked DRs added. (c) and (d) TE_{011} and quasi TE_{011} modes for a second configuration, empty cavity, and one with double-stacked DRs.

sensitivity of the experiments [3], [4], [19]–[26], at times up to roughly three orders of magnitude [23]. The field enhancement is greatest inside the DR itself, leading some to drill holes into the DRs or place their samples inside DRs with premade axial holes [20], [24], [25], [27]. Others have chosen to place their samples sandwiched between two DRs, and indeed, the two DR configuration has seen a lot of use—for example, in applications which require high pressure [28]–[30], optical access [2], or an increased field homogeneity outside of the DR [31]. The two DR configuration also allows for general tunability in both ESR and other applications, for example, by varying the spacing between the two DRs or placement of the DRs within the cavity [15], [32]–[37]. Some degree of tunability has also been obtained by exchanging the DRs with similar ones of different dimensions or dielectric constants in single or double DR configurations [2], [38].

Due to the significance of DRs and the lack of an analytic solution, a number of numerical techniques have been developed to calculate approximate resonant frequencies of DRs and DR-containing cavities. In rough chronological order, these include solving a transcendental equation through either the magnetic wall waveguide model [39]–[41], the dielectric waveguide model [42], [43], or a hybrid of the two [44]; using a variational procedure for approximating answers [45]; doing a surface integral implementation with method-of-moments [46], [47]; using effective dielectric constants [48], [49]; solving a matrix equation after expanding in terms of empty cavity modes [50]; and using coupled mode theory or a mode-matching technique [51], [52]. Often these methods require simple geometries, assume metal caps on top and bottom, place limitations on usable dielectric constants, and so on As an example, some useful formulas for predicting resonant frequencies for single and stacked DR configurations are given by Jaworski *et al.* [44] but the formulas are limited to dielectric constant $\epsilon_r \approx 30$ and DR aspect ratio between 0.4 and 1. To get more precise values of resonant frequency and/or the pattern of electric and magnetic fields, typically more sophisticated approaches are used, which can be time-consuming to implement and often require commercial software or sophisticated programming. These include finite integration [53]–[55], the finite-element method (FEM) [13], [56]–[58], and others [59]. Such approaches are sometimes used to check other theoretical or experimental work such as those cited above.

For this article, we have chosen to focus on the double-stacked DR configuration inside a conducting cavity, with two DRs symmetrically placed above and below the cavity midpoint, where each DR can additionally contain a central axial hole. We note that this is a very general configuration, which can even include single DRs (if the separation distance is set to zero) and DRs with no holes (if the DR inner diameter is set to zero).

The goal of this work was to develop a technique which is nearly as accurate as FEM, but which can run in a fraction of the time. To do this, we employed machine learning in the form of two independent neural networks, one of which learned to predict the resonant frequency of the quasi TE_{011} mode, the other of which learned to predict the electric field of the mode (from which the magnetic field can also be calculated). In order to train the neural networks, we developed our own FEM code using FEniCS in Python, based in large part on the work by Weickhmann [13]. In order to efficiently

represent information about the mode, we characterized the quasi TE_{011} mode in terms of empty cavity modes, similar to previous work by our group [50]. We solved for the quasi TE_{011} mode for 97 161 random configurations, added 2809 known configurations of fully filled cavities, and used the resulting 99 970 modes to train the two neural networks. We assessed the networks with 9564 independently solved holdout samples; results show that the trained neural networks are highly accurate and extremely fast, approximately 10 000× faster than the FEM calculations. The median error for the normalized frequency predictions is 0.2%. The median error in the field prediction is 0.003%, as defined by the projection of the electric field calculated by the FEM code onto the field calculated by the neural network. These results show not only that the trained neural networks excel at their job but also that electric field mode is in general a very learnable quantity via the expansion coefficient method.

II. Finite-Element Method

For creating the training samples for our neural network, we used FEniCS, an open-source package in Python for solving partial differential equations (PDEs) through FEM [60]. Generally, the FEM is able to numerically approximate some unknown function by expressing a PDE as a variational problem. In finite-element analysis, a weak form governing equation is a variational form of the original problem, by multiplying the trial function (the unknown function being approximated) by a test function which is zero on the boundary, integrating the resulting equation over the domain, and performing integration by parts if needed for terms with second-order derivatives [60].

In our case, the weak form governing equation is provided in the Appendix. It is turned into a generalized eigenvalue problem which FEniCS can solve, as is also demonstrated in the Appendix. The eigenvalues λ allow the resonant frequency of the mode to be obtained and the eigenvectors $\mathbf{e}$ give the coefficients (in terms of the finite-element basis functions) of the electric field for that mode. (The symbol λ here should not be confused with wavelength, as the eigenvalues relate to the wavenumber squared as detailed in the Appendix.)

Our FEniCS code solves for the resonant mode near an estimated target frequency. We use as our starting point a frequency below any of the resonant frequencies, and then adjust the target higher and higher until a resonant mode is found. As explained in the Appendix, our code can only find $m = 0$ modes. Our starting point is the resonant frequency of the TM_{010} mode for a cavity completely filled with the DR material, since: 1) the TM_{010} mode is always the lowest frequency mode of an empty or completely filled cavity when m is restricted to 0 and 2) the frequency of the lowest resonant mode of the actual cavity will necessarily be higher than the lowest frequency of a completely filled cavity since adding air pockets to a completely filled cavity only reduces the optical path length of the electromagnetic wave inside the cavity, thus increasing the frequency.

If no resonant mode is found near the target frequency, then our program increases the target frequency iteratively at a higher and higher rate until a resonant mode is found. Once a resonant mode is found, our program tests whether the found mode is quasi TE_{011} by sampling the electric field on a 50×50 grid over the domain and running two checks which ensure the topology of the mode matches the empty cavity TE_{011} mode; this guarantees the proper topology for the magnetic field as well. The desired topology is that the electric field should be only in the ϕ-direction and should never change direction. The first check is to make sure that the sum of $|E_\phi|$ over all points in the cavity is larger than the combined sums of $|E_r|$ and $|E_z|$ (which are small but due to numerical errors potentially nonzero). The second check is to make sure that E_ϕ is always positive, within some tolerance.

If the mode found by FEniCS fails either of the two tests, the program starts increasing the target frequency again (after resetting the increment rate) and looks for the next higher mode. The process continues until either the quasi TE_{011} mode is identified, or 12 nonquasi TE_{011} modes are found, in which case the program gives up. This only happens rarely for reasonable cavity configuration choices such as those described by the parameters in Section IV.

A calculation for a typical cavity configuration takes on average about 30 min of supercomputer time, running on a node of the BYU "marylou8" cluster, with the node using a 12-core Intel Haswell (2.3 GHz) processor and 100 GB of memory.

III. Parametrizing the Quasi TE_{011} Mode for Machine Learning

In order to assist the machine learning algorithm in efficiently finding the quasi TE_{011} mode, we express the mode as a linear combination of empty cavity modes, as per (1). This is similar to a method employed previously by our group [50], although in that work the $\mathbf{D}$ field was expressed in the expansion rather than the $\mathbf{E}$ field. Incidentally, the $\mathbf{E}$ field was used in this current work rather than the $\mathbf{D}$ field due to our inability to obtain a solvable weak form FEM equation for $\mathbf{D}$. The expansion is

$$\mathbf{E} = \sum_{\text{lmnp}} a_{\text{lmnp}} \mathbf{E}_{\text{lmnp}}. \tag{1}$$

In this equation, $\mathbf{E}_{\text{lmnp}}$ refers to a resonant mode of an empty cavity having the same dimensions as the dielectric-filled cavity, with $l = 0$ or 1 referring to TE or TM, respectively, and m, n, and p being the azimuthal, radial, and longitudinal mode numbers. The quasi TE_{011} mode can be constructed solely from TE modes having $m = 0$; therefore, we restrict the summation to $l = m = 0$. For a known field $\mathbf{E}$, the coefficient of the TE_{0np} term can be obtained by starting with (1) and applying "Fourier's trick" of dotting the field into the complex conjugate of $\mathbf{E}_{\text{lmnp}}$, integrating over the domain, then using the orthogonality condition. Doing so, we obtain

$$a_{\text{lmnp}} = \frac{\int_\Omega \mathbf{E}^*_{\text{lmnp}} \cdot \mathbf{E}\, dV}{\int_\Omega \mathbf{E}^*_{\text{lmnp}} \cdot \mathbf{E}_{\text{lmnp}}\, dV}. \tag{2}$$

The denominator can be evaluated using the electric field components of the TE modes of an empty cylindrical cavity

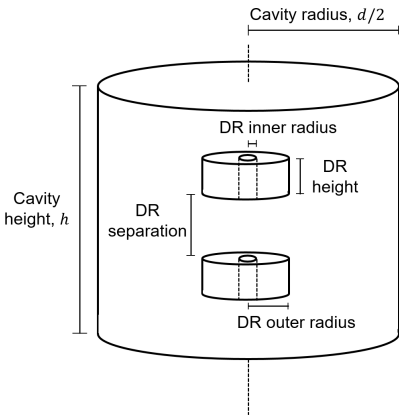

Fig. 2. Geometry of the double-stacked DR configuration.

from, e.g., [61], to obtain the following:

$$a_{00\,\mathrm{np}} = \frac{1}{\frac{h\pi R^2}{2}\left(1+\left(\frac{p\pi R}{h j_{1n}}\right)^2\right) J_0^2(j_{1n})} \times \int_\Omega \mathbf{E}^*_{00\,\mathrm{np}} \cdot \mathbf{E}\, dV. \quad (3)$$

Here, h and R are the cavity height and radius, respectively, j_{1n} is the nth zero of the first Bessel function, $\mathbf{E}_{00\,\mathrm{np}}$ is the empty cavity field for the $\mathrm{TE}_{0\,\mathrm{np}}$ mode, and $\mathbf{E}$ is the field of the actual cavity for the resonant mode obtained by our FEniCS code.

By investigating several representative physical configurations for dual stacked DRs inside a cylindrical cavity, we compiled a list of the 200 most significant $\mathrm{TE}_{0\,\mathrm{np}}$ empty cavity modes, in order, the first ten of which are TE_{011}, TE_{021}, TE_{013}, TE_{031}, TE_{041}, TE_{015}, TE_{023}, TE_{051}, TE_{017}, and TE_{061}. Note that the symmetry of the cavity requires p to be odd for the quasi TE_{011} mode. Typically, the TE_{011} coefficient, namely, a_{0011}, is the largest of the 200 coefficients in magnitude for the quasi TE_{011} mode; however, in approximately 10% of the parameter sets we investigated, some other coefficient was larger.

The integrals to obtain the $a_{00\,\mathrm{np}}$ coefficients were performed using 200×200 sampling grids of the field found by FEniCS, and the coefficients for a given field are normalized such that the sum of their squares equals 1.

IV. Creating Training Samples

The FEM program described in Section II can be used with only small modifications for any cylindrically symmetric cavity configuration, as defined by the ϵ_r spatial function within the code. For the purposes of developing a machine learning algorithm, however, we limited the physical geometry to the double-stacked DR configuration as indicated in Fig. 2. Such a geometry can be completely specified with seven parameters: cavity diameter (or radius) and height, inner and outer radii of the DRs, height of the DRs, vertical distance separating the DRs, and the dielectric constant of the DRs.

Two physical cavities which differ only by a scaling factor in all dimensions will have an identical field pattern and will differ in frequency only by that same scaling factor. Therefore, the machine learning can be made substantially much more efficient by considering only normalized cavities having the same size (using a consistent measure of cavity size), as long as the frequency of the desired cavity can be recovered from the frequency of a normalized cavity. Using normalized cavities also removes one degree of freedom from the cavity parameters: cavities are specified using six parameters instead of seven.

TABLE I
List of Neural Network Inputs and Outputs

Inputs (6)	Outputs (201)
Aspect ratio of cavity DR inner radius DR outer radius DR height DR separation DR ϵ_r	Neural net 1: Normalized frequency Neural net 2: Expansion coefficients of empty cavity modes, i.e. 200 a_{00np} values

The measure of cavity size we have chosen to use is the harmonic mean of the height and diameter, hereafter referred to simply as "harmonic mean," or HM. The HM and cavity aspect ratio AR together determines the cavity height h and diameter d, according to the following equations:

$$\mathrm{AR} = \frac{h}{d} \quad (4)$$

$$\mathrm{HM} = \frac{2hd}{h+d} \quad (5)$$

and the inverse equations

$$h = \frac{1+\mathrm{AR}}{2}\mathrm{HM} \quad (6)$$

$$d = \frac{1+\mathrm{AR}}{2\mathrm{AR}}\mathrm{HM}. \quad (7)$$

We enforce the condition $\mathrm{HM} = 1$ when creating our training samples. Our FEM program additionally sets the speed of light to unity for convenience and, therefore, outputs a dimensionless normalized frequency. To recover the actual frequency in Hz for real-world situations where the harmonic mean is not unity, we normalize all other physical dimensions by dividing by HM, and use the following relationship:

$$f = \frac{f_{\mathrm{norm}} c}{\mathrm{HM}} \quad (8)$$

where c being the speed of light in m/s and HM being the harmonic mean in meters.

As indicated in Table I, one sample of training data consists of the inputs which are the six parameters specifying the cavity geometry, and the outputs which are the normalized frequency and the 200 $a_{00\,\mathrm{np}}$ values describing the quasi TE_{011} field.

To sample the 6-D parameter space, we employed Latin hypercube sampling (LHS), which is a statistical method to ensure each region of a multivariable distribution is sampled with near-random values. Each variable is partitioned into N nonoverlapping intervals. One value is selected at random from each interval and randomly matched with a value from an interval of each other variable. This is done over the whole distribution in such a way that each interval of each variable is used exactly once. With two variables and visualizing the

partitioned intervals as rows and columns, the sampling for $N = 8$ is equivalent to positioning rooks on an 8×8 chess board in such a way that no two rooks can threaten each other. There will be exactly one rook (one sample point) in each row and in each column, with eight total rooks. Hence, the number of sample points is equal to the number of partitioned intervals. A Latin hypercube is the generalization of this concept to an arbitrary number of dimensions, e.g., a 6-D chessboard for our case. This stratified sampling method offers coverage of the whole multivariable distribution while maintaining a component of randomness suitable for machine learning datasets [62], [63]. We implemented LHS over the input variables for our neural network using the Surrogate Modeling Toolbox package in Python.

The LHS points are returned as sets of six numbers from 0 to 1, call them $p_1, \ldots, p_6$, which then must be rescaled to correspond to our six parameters. We did that as follows. To generate the aspect ratio, p_1, was rescaled to be between 0.25 and 4, using a log scale so there would be the same number of aspect ratios less than 1 as above 1. Based on (6) and (7), the cavity's height and diameter were then calculated with an enforced harmonic mean of 1. The smallest aspect ratio of 0.25 corresponds to a cavity height and diameter of 0.625 and 2.5, respectively; the largest aspect ratio of 4 corresponds to the reverse, that is to say, cavity height and diameter of 2.5 and 0.625. The DR inner and outer radii were then generated by rescaling p_2 and p_3 to be from 0 to the cavity radius, swapping the two if $p_2 > p_3$. The DR height was generated by rescaling p_4 to be from 0 to half the cavity height. The parameter set was thrown out if either the DR annular radius (difference of outer and inner radii) or the DR height resulted in a value which was too small for the mesh resolution we employed, namely, 1/100 of the larger of the two cavity dimensions. The DR separation distance was generated by rescaling p_5 to go from 0 to $h_{\text{cavity}} - 2h_{\text{DR}}$, to guarantee that the DRs fit completely within the cavity. Finally, the dielectric constant was generated by rescaling p_6 to go from 1 to 45, that marking the approximate upper limit of commercially available DRs, and additionally skewing the distribution away from the lowest values because: 1) the low dielectric constant DRs take longer to calculate due to a larger difference between initial target frequency and the actual quasi TE_{011} resonant frequency and 2) very small dielectric constant values are less likely to be employed in practice.

That process was repeated for each set of $p_1, \ldots, p_6$ generated by the LHS code, and resulted in 97 161 sets of usable cavity parameters which we used for developing our neural network. Histograms of the cavity parameters are shown in Fig. 3. An additional independently sampled 9564 points generated the same way were created as a holdout dataset to determine the quality of our neural network. Those 106 725 total sets of parameters were then run through our FEM code to determine the normalized frequency and empty cavity expansion coefficients for each one; this took approximately 53 000 CPU hours of supercomputer time. After the network architecture was established as described in this section, an additional 2809 samples of known data in the form of completely dielectric filled cavities—where exact analytic solutions are known—were added, forming 99 970 total training samples.

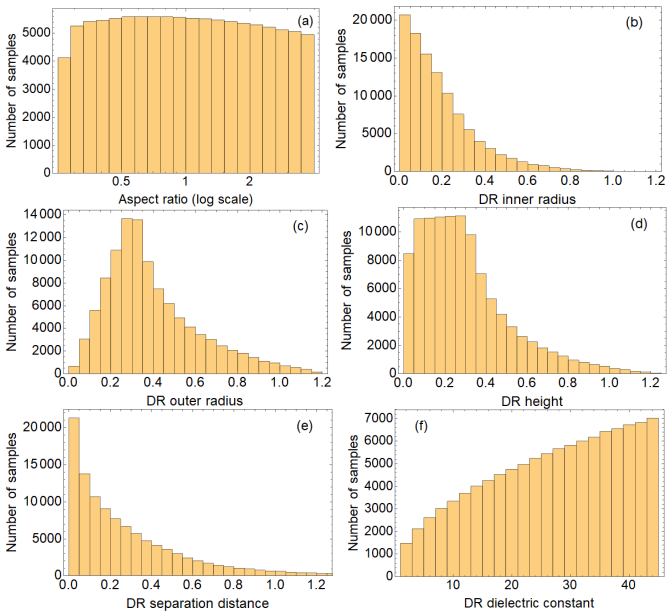

Fig. 3. Histograms of the six parameters in the 106 725 samples used for training and evaluating the neural network: (a) aspect ratio (shown on a log scale), (b) DR inner radius, (c) DR outer radius (OR), (d) DR height, (e) DR separation distance, and (f) dielectric constant. All distances are normalized such that HM as defined by (5) equals unity.

V. Neural Network Training, Development, and Results

We developed two independent neural networks, one of which learned to predict the resonant frequency of the quasi TE_{011} mode for any given set of input parameters, the other of which calculated the 200 $a_{00\,\text{np}}$ empty cavity mode coefficients. In each case, a random 80–20 split of the samples was done to form training and testing/validation sets and develop the neural networks. Both networks were developed using mean squared error loss functions (which for the coefficient-predicting neural network means average of the sum of the squared errors of all of the coefficients). We used the Keras API with Tensorflow backend in Python for all of the neural network programming. Optimal hyperparameters such as number and type of layers, activation functions, optimizer, learning rate, and number of training epochs, were found using standard procedures.

Comparisons between some selected networks and hyperparameters can be found in Table II. The dense neural networks (DNNs) in Table II follow the same architecture as presented below. The convolutional neural networks (CNNs) in Table II have two convolutional layers, flattened and followed by two dense layers. The bolded row indicates what we used for the final networks.

Fig. 4 presents summaries of the final architectures of each of the two networks. The final frequency-predicting neural network is comprised of six fully connected layers with 256, 128, 64, 32, 16, and 1 nodes. The first five layers use the "swish" activation function defined by $f(x) = x\text{sigmoid}(x)$. The output layer uses a linear activation function. Other hyperparameters are as follows: Adam optimizer, initial learning

TABLE II
COMPARISON OF SELECTED NEURAL NETWORKS

	Mean squared error of holdout set	
	Frequency network	Coefficient network
CNN (swish activation, learning rate scheduler)	1.22×10^{-4}	9.93×10^{-6}
DNN (swish activation, learning rate scheduler)	$\mathbf{2.66 \times 10^{-5}}$	$\mathbf{2.98 \times 10^{-6}}$
DNN (swish activation)	3.08×10^{-4}	1.30×10^{-5}
DNN (relu activation, learning rate scheduler)	9.71×10^{-5}	4.41×10^{-4}
DNN (swish activation, learning rate scheduler, dropout layers)	3.58×10^{-3}	5.72×10^{-4}

rate of 0.005, and a batch size of 50. The final expansion coefficient-predicting neural network is comprised of seven fully connected layers with 2048, 1024, 512, 256, 256, 256, and 200 nodes. After these, a lambda layer is used to enforce L2 normalization of the coefficient array. Swish activation functions are used for all layers. Other parameters chosen for this network include Adam optimizer, initial learning rate of 0.0005, and a batch size of 25.

Both networks were trained using three callbacks: EarlyStopping, ModelCheckpoint, and LearningRateScheduler. EarlyStopping, implemented with a patience of 150 for the frequency network, 75 for the coefficients network, and a minimum delta of 10^{-5}, ensured that little time was wasted on unproductive training. That is to say, if the loss function failed to improve by at least 10^{-5} in the given number of consecutive epochs, training was stopped early. ModelCheckpoint made sure that a new version of the network was saved only when the error metric improved. After a specific number of epochs, LearningRateScheduler began decreasing the learning rate according to the following formula: $\mathrm{LR}_{\mathrm{new}} = \mathrm{LR}_{\mathrm{old}} e^{-0.1}$. For the frequency network, this process started after 100 epochs; and 75 epochs for the coefficients network. Plots of the loss functions versus epoch for the two neural networks are included in Fig. 5. The two networks hit their EarlyStopping limits after 383 and 206 epochs, respectively.

Once the neural networks were developed, the holdout dataset was used to assess the performance of the final networks. A plot of all of the frequency errors for the 9564 holdout points is provided in Fig. 6(a); the median of the absolute values of the fractional frequency errors was 0.2%.

To assess the coefficient network, we have used a "similarity score" obtained by projecting the field predicted by the neural network onto the field generated by FEniCS, which due to the orthogonality of the empty cavity modes is just the dot product of the two vectors of coefficients

$$\text{Similarity score} = \int \mathbf{E}^*_{\text{FEniCS}} \cdot \mathbf{E}_{\text{neural net}}\, dV = \sum a_{00\,\text{np,FEniCS}}\, a_{00\,\text{np,neuralnet}}. \quad (9)$$

A similarity score of 100% means the two fields are identical, whereas a score of 0% would indicate no similarity between fields. A plot of the field errors (1—similarity score) for the holdout points is provided in Fig. 6(b). The overall ability of the neural network to correctly predict the electric field of the quasi TE_{011} mode is remarkable! The median similarity score of the 9564 holdout points is 99.997%, which is to say a 0.003% error in the field; and all but seven of the 9564 points have a similarity score of 99% or higher. There is a trend indicating the neural network does not predict the

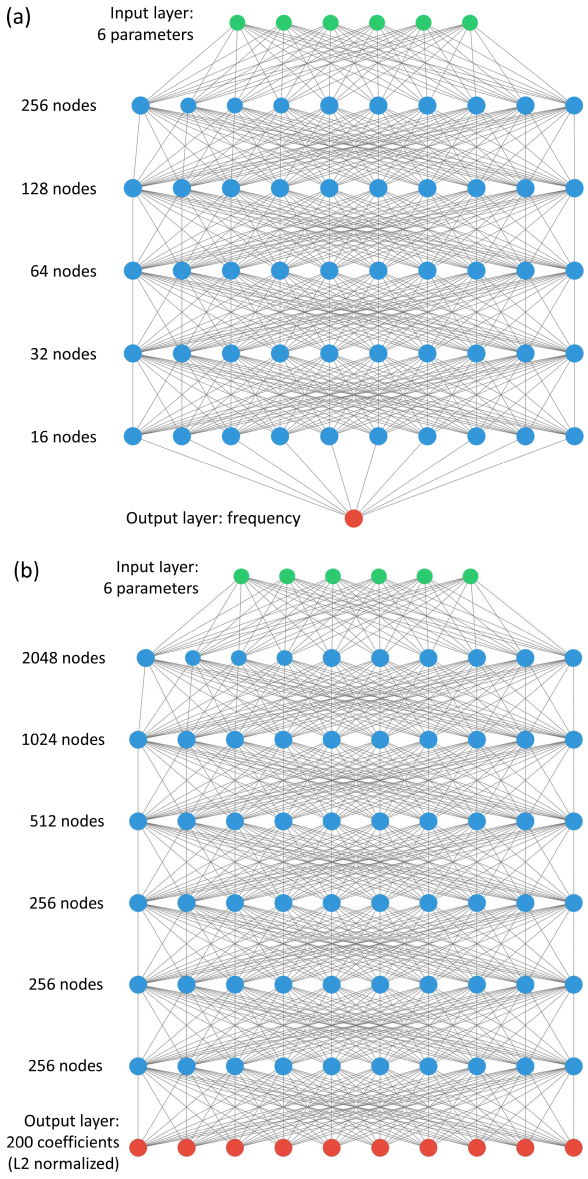

Fig. 4. Schematic depiction of the final architectures of (a) frequency-predicting and (b) expansion coefficient-predicting neural networks.

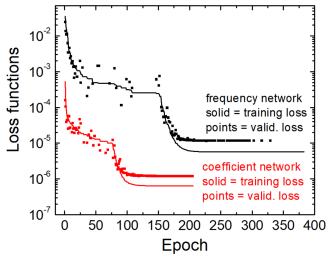

Fig. 5. Loss functions versus training epoch for the two neural networks. The solid lines are the loss functions for the training sets; the scatter points are the loss function of the testing/validation sets displayed at selected points, namely, the points at which the training loss improved.

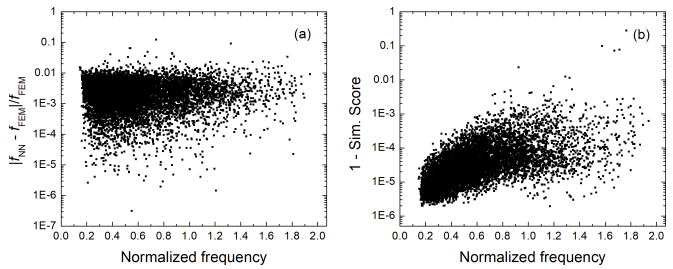

Fig. 6. Results of the two neural networks for the 9564 holdout points: (a) absolute value of the fractional error of the predicted normalized frequency, plotted versus the normalized frequency given by FEM. The median absolute fractional error of frequency is 0.2% and (b) deviation from 1 of the similarity score of the empty cavity $a_{00\,\mathrm{np}}$ expansion coefficients, plotted versus the normalized frequency given by FEM. The median similarity score is 99.997% (i.e., median deviation from unity is 3×10^{-5}).

mode quite as well for large frequencies [$r = 0.599$ and $p < 0.0001$ from a linear regression of the log-linear data of Fig. 6(b)]; nevertheless, the extremely low errors demonstrate that the empty cavity modes are remarkably well suited as basis functions for this type of machine learning.

Running the two neural networks to establish the frequency and expansion coefficients for a given set of cavity parameters takes roughly 0.07 s for each network running on a typical personal computer, a speedup of approximately 10 000× compared with our FEniCS code.

Analyzing the coefficient neural network performance a bit further through linear regressions using log–log plots, we find the following, with $p < 0.0001$ for all of these results. The neural network performed better for aspect ratios toward the center of the range ($r = -0.118$ when analyzing AR < 1; $r = 0.275$ when analyzing AR > 1). The neural network performed better for smaller DR separations ($r = 0.362$) and only very slightly better for smaller DR ϵ_r ($r = 0.054$). So far, the most significant factors were the DR annular radius (DR OR − DR inner radius) and DR height: when judged as a fraction of the cavity radius and cavity height, respectively, the neural networks performed substantially better for larger annular radii and larger heights ($r = 0.478$ and $r = 0.594$, respectively). In other words, the neural network is at its best when the DRs are not too thin in either dimension. Interestingly, the frequency neural network shows far milder trends for small DR annular radius and height than the coefficient network, perhaps because using thin DRs should cause the quasi TE_{011} mode frequency to become close to the empty cavity TE_{011} frequency.

As another assessment of how the neural networks perform at the limits of the trained parameter space, we have tested the networks for a random selection of 3000 fully filled cavities, for which exact solutions to frequency and mode are known. This was done for a range of aspect ratios from 0.125 to 8, i.e., including aspect ratios both less than and greater than our trained region by factors of two; and dielectric constants from 1 to 90, i.e., greater than our trained region by a factor of two. For parameters inside our trained region, the frequency and field errors were 0.2% and an incredible 0.00007%, respectively; and for parameters outside the trained region, the errors were 4.7% and 0.002%, respectively. As would be expected, the largest errors came at the limits of the aspect ratios (especially those close to 0.125) and dielectric constants. In particular, when dielectric constant was greater than 45, there is a very large correlation between large errors and large dielectric constants ($r = 0.818$).

We have additionally explored the behavior of the frequency network for some parameters outside of the trained region, in a more standard double-stacked DR configuration. Typically the neural network provides plausible, although presumably incorrect, values when one is not too far away from the trained region. For example, when the DR height is too large to fit into the cavity, the predictions are reasonable although perhaps not physically meaningful. In looking at DR height and annular widths which are too small for the trained region (due to limits of FEM mesh size, as mentioned in the Appendix), the frequency predictions are also somewhat reasonable, in the sense that they are close to predictions at the limits of the trained region. However, as some parameters get farther and farther away from the trained region, eventually the neural network stops predicting meaningful values and the frequencies even go negative (e.g., for aspect ratios above about 8 and dielectric constants above about 200, in one test).

Resonant cavities are often characterized by the Q-factor, a measure of the sharpness of the resonance, and degree of cavity loss. Because our methods assume perfectly conducting walls and a lossless dielectric, the Q-factor in our calculations is in some sense infinite. Instead, we use the magnetic filling factor (FF), an important parameter for spin resonance experiments in particular, which is equal to the magnetic field's energy integrated over the volume occupied by the sample, divided by the total magnetic field energy in the cavity. One can show that in the limit of a negligibly small sample placed in the cavity center, the FF becomes

$$\mathrm{FF} \sim \frac{V_{\mathrm{cavity}} |\mathbf{B}(\mathbf{r}=0)|^2}{\sum |b_{\mathrm{lmnp}}|^2} \tag{10}$$

where b_{lmnp} are the expansion coefficients of the magnetic field $\mathbf{B}$ in terms of the empty cavity magnetic field modes; it can be shown that $b_{\mathrm{lmnp}} = \omega_{\mathrm{lmnp}}/\omega$ with ω_{lmnp} indicates the resonant frequency of the corresponding empty cavity mode and ω indicates the resonant frequency of the actual mode. (The formula for b_{lmnp} appears as the reverse of (20) of [50] because in that work it is the $\mathbf{D}$ field which is expanded in empty cavity modes.) To assist with cavity design, our neural network Python code also outputs the result of (10) for the specified parameters, which we call the "scaled FF." To recover the actual FF, one must multiply the scaled factor, (10), by the ratio of the sample volume to cavity volume.

VI. Application Example and Comparison With Experiments

As an illustration of an application of the neural network, we present the following analysis of a situation where we have defined an overall cavity of height 35.65 mm and diameter 14.18 mm, to match the physical cavity of [50] for comparison, and then experiment with how the DR properties affect the resonant frequency and scaled FF of the quasi TE_{011} mode.

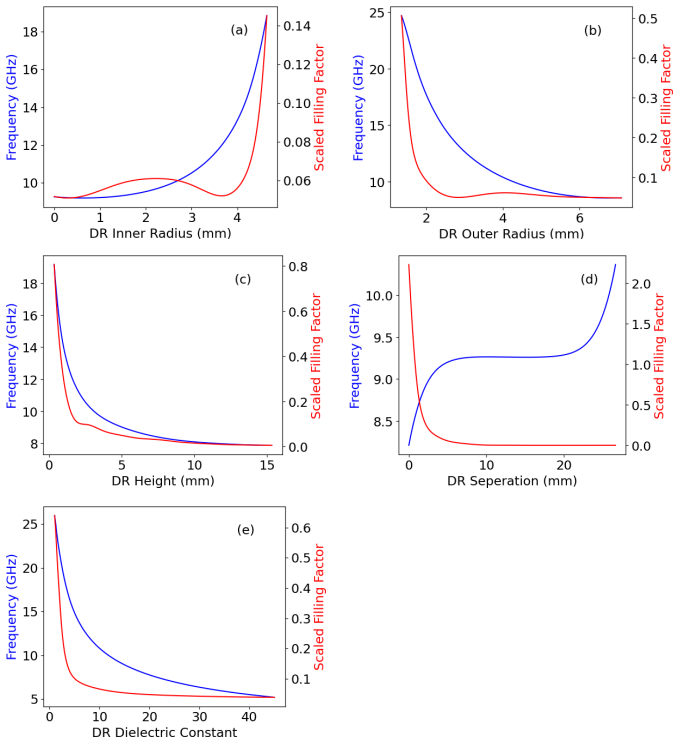

Fig. 7. Results of neural network frequency and scaled FF calculations for a configuration similar to [50], namely, an overall cavity of height 35.65 mm and diameter 14.18 mm. In each of the graphs (a)–(e) one of the parameters is varied (DR inner radius, DR OR, DR height, DR separation, and DR dielectric constant, respectively, as indicated by the x-axis), while the nonvarying parameters are held constant at these values: DR inner radius = 1 mm, DR OR = 5 mm, DR height = 4.5 mm, DR separation distance = 5 mm, and $\epsilon_r = 14$.

In each of the graphs in Fig. 7, one of the parameters is varied (as indicated by the x-axis), while the nonvarying parameters are held constant at these values: DR inner radius = 1 mm, DR OR = 5 mm, DR height = 4.5 mm, DR separation distance = 5 mm, $\epsilon_r = 14$. To obtain the frequency for a given set of parameters, we normalize all dimensions according to the harmonic mean of cavity height and diameter, feed the values into the frequency neural network, obtain the dimensionless normalized resonant frequency back, and then rescale according to (8) to obtain the physical frequency in Hz. The process is repeated for 200 values across each of the x-axis to form the curves shown in Fig. 7. Again to emphasize the tremendous speedup offered by the neural network, each of these frequency plots takes roughly 14 s to generate—or roughly double that if the FF is also plotted, as in that case the expansion coefficients must also be calculated—as compared with approximately 100 h if we were calculating 200 different configurations via FEniCS.

This type of analysis could be useful, for example, when DRs are added to a cavity in order to target a particular frequency, or when tunability is obtained by varying parameters such as the DR separation distance as in the design of Sienkiewicz *et al.* [37] and Mattar and Elnaggar [36] (which is discussed further below), which allow frequencies to be altered in a ∼1–2-GHz range. The work of Khalajmehrabadi *et al.* [15] similarly involves a study of how frequencies vary as DR parameters are changed, in their case, DR thickness and dielectric constant.

TABLE III
COMPARISON WITH EXPERIMENT

	Experimental and Computed Frequencies (GHz)				
DR height (mm)	Jaworski (no Rex.)	Neural Net (no Rex.)	FEM (no Rex.)	FEM (with Rex.)	Experiment
1.5	11.420	12.304	12.374	11.826	11.750
3	9.283	10.072	10.105	9.8846	10.080
4.5	8.399	9.200	9.1861	9.0457	9.039
6	7.921	8.712	8.6963	8.5880	8.628
7.5	7.626	8.387	8.3979	8.3062	8.346

Since real-world applications typically involve additional dielectric material inside the cavities, such as Rexolite supports [2], [4], [13], [30], [33], [37], [44], [50], [65], [66], we suggest that designers could combine our neural network and FEM programs—using the neural network to first obtain a desired result by analyzing hundreds or thousands of configurations of stacked DRs in an otherwise empty cavity, then double-checking the chosen configuration with a single final (slow) calculation using our FEM code in which additional dielectric material can easily be incorporated. This is quite similar to what has been done by Hyde and Mett [64], in a work involving a single DR extending axially from cavity wall to cavity wall—they used contour plots of dimensions of the metallic cylinder, developed using analytical equations, to find a cavity with a resonance at 9.5 GHz and then confirmed that by time-consuming finite-element modeling [64]. (As a parenthetical note, their design of a DR filling the cavity axially, which as they pointed out distinguishes their work from the extensive body of work on DRs, falls under the parameter ranges covered by our neural network simply by setting the OR equal to the cavity radius.)

We present some results using this approach in Table III, where we compare with experimental data from [50] obtained by varying the DR height. The columns include our neural network calculations, which incidentally are five points from Fig. 7(c), followed by FEM calculations assuming only DRs in the cavity, followed by FEM calculations with Rexolite supports as described in [50], then finally the experimental measurements. The neural network matches the FEM without Rexolite calculations extremely well, with a median absolute value error of 0.2%, and the FEM with Rexolite calculations match the experimental measurements also extremely well, with a median absolute value error of 0.5%. For additional comparison, a column giving the (much less accurate) results of Jaworski *et al.* [44] for stacked DRs in an otherwise empty cavity has also been included as a commonly used approximation.

VII. COMPARISON WITH OTHER METHODS

We now present a comparison of our neural network with several other calculations for the configuration of Mattar and Elnaggar [36], which is two stacked DRs having ϵ_r of 29.2, DR height of 2.65 mm, DR inner radius of 0, DR OR of 3 mm, and a variable DR separation; placed in a cavity with height $h = 41$ mm and diameter $d = 41$ mm (i.e., AR = 1). Mattar *et al.* use an energy-coupled mode theory (ECMT) to obtain an approximation for the cavity mode and resonant

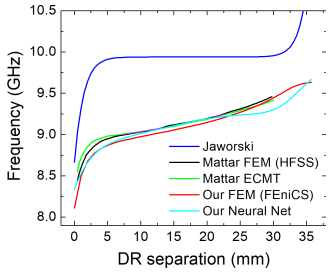

Fig. 8. Frequency versus separation distance for the configuration of [36], using various techniques: HFSS (a commercial FEM solver; black), ECMT (green), our FEM code (red), our neural network (cyan), and the Jaworski method from [44] (blue). The data for the black and green curves are from [36].

frequency by computing coupling coefficients describing the overlap of fields of isolated DRs and of DRs and cavity [51]. In that work, they also use HFSS (a commercial FEM solver) to compute the modes and frequencies for comparison. In Fig. 8, we present their ECMT and HFSS solutions as DR separation distance is varied, along with the results from our own FEM code (FEniCS) and our neural network. As in Table III, we additionally present results from the method of Jaworski *et al.* [44] for comparison.

From Fig. 8, one can see the FEM, ECMT, and neural network curves are all in reasonably good agreement with each other ($\pm 0.5\%$ over most of the range); however, the neural network has increased error for some of the larger separation distances ($\sim$1.4% error in the 29–33-mm range). We believe that this is just coincidentally a bad region of our trained parameter space. This corresponds to configurations where the dielectrics are very close to the ends of the cavity, which could especially perturb the fields as the distance from the cavity wall is varied, and we did not have a great many sampled training points under such conditions. Therefore, even though the holdout points under those conditions did not display a significant error, the frequency neural network is apparently slightly mismodelling this region of parameter space.

To conclude this comparison, we note that one downside of the ECMT technique is that the fields of isolated DRs must be known in order to compute the overlap integrals. The fields are not analytically solvable, and so some other technique must be used in order to obtain them. Our neural network technique has the large advantage of being stand-alone.

VIII. Conclusion

In conclusion, we have developed two neural networks, to predict the resonant frequency and the field pattern of the quasi TE_{011} mode of a cylindrical microwave cavity with double-stacked DRs. The neural network was trained and evaluated with more than 100 000 samples created using a supercomputer to solve random cavity configurations via FEM implemented via FEniCS in Python. The neural networks are extremely accurate (0.2% median error in frequency predictions) and quick (speedup of approximately 10 000$\times$ compared with FEM calculations), and these results indicate that the empty cavity modes which we have employed as a basis form of a machine learnable set of functions. This machine learning technique could be extended to other modes and geometries, such as annular stacked DRs [52], side-by-side DRs [67], or even rectangular microwave cavities (although the FEniCS code would need to be substantially altered to generate training samples in a noncylindrically symmetric case).

Appendix
Derivation of Weak Form Equation

To obtain the weak form equation for use with FEM, we follow in large part the derivations of [13] and [68]. Maxwell's equations for a linear, isotropic, ohmic medium where $\mathbf{D} = \epsilon \mathbf{E}$, $\mathbf{H} = (1/\mu)\mathbf{B}$, and $\mathbf{J_f} = \sigma \mathbf{E}$ are the following:

$$\begin{aligned} \nabla \cdot \epsilon \mathbf{E} &= \rho_{\mathrm{f}} \\ \nabla \times \mathbf{E} &= -\mu \frac{\partial \mathbf{H}}{\partial t} \\ \nabla \cdot \mu \mathbf{H} &= 0 \\ \nabla \times \mathbf{H} &= \epsilon \frac{\partial \mathbf{E}}{\partial t} + \sigma \mathbf{E}. \end{aligned} \tag{A.1}$$

We assume $\rho_{\mathrm{f}} = 0$, $\mu = \mu_0$, and harmonic fields so $(\partial/\partial t) = i\omega$. Taking the curl of Faraday's law results in

$$\nabla \times \nabla \times \mathbf{E} = \omega^2 \epsilon \mu_0 \mathbf{E} - i\omega\mu_0 \sigma \mathbf{E}. \tag{A.2}$$

In order to obtain the weak form governing equation for use with the FEM, we take the inner product on the domain Ω with test function $\mathcal{E}$

$$\int_\Omega (\nabla \times \nabla \times \mathbf{E}) \cdot \mathcal{E}\, dV = \omega^2 \mu_0 \int_\Omega \epsilon(\mathbf{r}) \mathbf{E} \cdot \mathcal{E}\, dV - i\omega\mu_0 \int_\Omega \sigma(\mathbf{r}) \mathbf{E} \cdot \mathcal{E}\, dV. \tag{A.3}$$

Note that ϵ and σ are functions of the spatial coordinates, and are now explicitly written as such and, therefore, cannot be removed from the integrals.

To simplify the left-hand side of (A.3), we first note that the vector identity $\nabla \cdot (\mathbf{a} \times \mathbf{b}) = \mathbf{b} \cdot (\nabla \times \mathbf{a}) - \mathbf{a} \cdot (\nabla \times \mathbf{b})$, when used with $\mathbf{a} = \nabla \times \mathbf{E}$ and $\mathbf{b} = \mathcal{E}$, results in an equation which, when integrated over the domain and with the divergence theorem applied to the last term, results in

$$\int_\Omega (\nabla \times \nabla \times \mathbf{E}) \cdot \mathcal{E}\, dV = \int_\Omega (\nabla \times \mathbf{E}) \cdot (\nabla \times \mathcal{E})\, dV + \int_{\mathrm{d}\Omega} (\nabla \times \mathbf{E} \times \mathcal{E}) \cdot \hat{n} dS. \tag{A.4}$$

From the standard boundary conditions, the right most term in (A.4) can be neglected if we restrict ourselves to a perfectly electric and magnetic conducting boundary and ignore radiative losses [68]. Combining the nonzero terms of (A.4) with (A.3), and additionally using $\epsilon\mu_0 = \epsilon_r/c^2$, we obtain

$$\int_\Omega (\nabla \times \mathbf{E}) \cdot (\nabla \times \mathcal{E})\, dV = \frac{\omega^2}{c^2} \int_\Omega \epsilon_r(\mathbf{r}) \mathbf{E} \cdot \mathcal{E}\, dV - i\omega\mu_0 \int_\Omega \sigma \mathbf{E} \cdot \mathcal{E}\, dV. \tag{A.5}$$

For a dielectric filled cavity with conducting walls, the conductivity function $\sigma = 0$ over the domain Ω for a lossless medium and the field $\mathbf{E} = 0$ on the boundary $d\Omega$ according to the previous boundary condition. Therefore, the integrand

of the rightmost term of (A.5) is zero everywhere over the domain of the integral, and the weak form or variational form of the original boundary-value problem is

$$\int_\Omega (\nabla \times \mathbf{E}) \cdot (\nabla \times \mathcal{E})\, dV = \frac{\omega^2}{c^2} \int_\Omega \epsilon_r(\mathbf{r}) \mathbf{E} \cdot \mathcal{E}\, dV. \quad \text{(A.6)}$$

The weak form can then be turned into a matrix eigenvalue equation by discretizing the fields in the function space and then minimizing the functional [68], [69]. Due to the assumption of azimuthal symmetry, the problem can be decomposed into a Nédélec space for the r and z components and a continuous Galerkin or Lagrange space for the ϕ component [13]. As such, the electric field $\mathbf{E}$ is approximated on $\boldsymbol{\Omega}$ using 2-D curl-conforming basis functions $\mathbf{N}_j$ and nodal scalar basis functions L_j, as

$$\mathbf{E}_{rz} \approx \sum_{j=1}^{N} (e_{rz})_j \mathbf{N}_j \quad E_\phi \approx \sum_{j=1}^{N} (e_\phi)_j L_j \quad \text{(A.7)}$$

where N is the number of bases in the finite element framework and e_{rz} and e_ϕ the sets of unknown expansion coefficients for the (r, z) and ϕ-directions, respectively [69]. It should be noted that this set up may lead to spurious modes [58]; however, the quasi TE_{011} mode checks eliminate any spurious modes as possible solutions.

Substituting the discretized field equations into the weak form equation of (A.6) and applying a minimization procedure give the matrix equation

$$\begin{pmatrix} S_{rz} & 0 \\ 0 & S_\phi \end{pmatrix} \begin{pmatrix} e_{rz} \\ e_\phi \end{pmatrix} = \lambda \begin{pmatrix} T_{rz} & 0 \\ 0 & T_\phi \end{pmatrix} \begin{pmatrix} e_{rz} \\ e_\phi \end{pmatrix} \quad \text{(A.8)}$$

where S_{rz}, S_ϕ, T_{rz}, and T_ϕ each represent $N \times N$ matrices, given below in (A.10) through (A.13), and e_{rz} and e_ϕ each represent length N vectors.

This can be recognized as a generalized eigenvalue problem of the form

$$\overleftrightarrow{\mathbf{S}} \cdot \mathbf{e} = \lambda \overleftrightarrow{\mathbf{T}} \cdot \mathbf{e} \quad \text{(A.9)}$$

where S and T represent the stiffness and mass matrices. The i, j components of the four matrices are defined as [68], [69]

$$(S_{rz})_{ij} = \int_\Omega (\nabla_{rz} \times \mathbf{N}_i) \cdot (\nabla_{rz} \times \mathbf{N}_j)\, dV \quad \text{(A.10)}$$

$$(S_\phi)_{ij} = \int_\Omega (\nabla_\phi L_i) \cdot (\nabla_\phi L_j)\, dV \quad \text{(A.11)}$$

$$(T_{rz})_{ij} = \int_\Omega \epsilon_r(\mathbf{r}) \mathbf{N}_i \cdot \mathbf{N}_j\, dV \quad \text{(A.12)}$$

$$(T_\phi)_{ij} = \int_\Omega \epsilon_r(\mathbf{r}) L_i L_j\, dV. \quad \text{(A.13)}$$

In these equations, ∇_{rz} and ∇_ϕ represent the (r, z) and ϕ parts of the curl or gradient operations as indicated.

The computations are greatly sped up by enforcing azimuthal symmetry in cylindrical coordinates, namely $dV = 2\pi r dr dz$, turning the 3-D finite-element problem into a 2-D problem using a grid over r and z (and in practice nearly all factors of 2π are canceled out of our code). This has the additional effect of restricting the solutions to modes with azimuthal mode number $m = 0$, which have no ϕ dependence.

The eigenvector $\mathbf{e}$ in the generalized matrix equation (A.9) is the vector of the expansion coefficients, and the eigenvalue λ corresponds to a resonant frequency ω via

$$\lambda = \frac{\omega^2}{c^2}. \quad \text{(A.14)}$$

We can obtain the resonant frequency f from the eigenvalue via $f = c(\lambda)^{1/2}/2\pi$. Note that λ here is not wavelength but rather a generic symbol for eigenvalue. For computational simplicity, we have used $c = 1$ in our code. To recover frequency in Hz, use (8).

The FEniCS-specific implementation is done by first using the FEniCS-related packages mshr and DOLFIN to define the dimensions of the cavity and create a rectangular 2-D mesh representing r and z dimensions. The mesh is created via the command: mesh = generate_mesh (domain, 100), where the argument of 100 indicates we would like to resolve the geometry with 100 cells across the larger dimension. Consequently, we only trust the FEniCS results with DRs as small as approximately 1/100 of the larger of the two cavity dimensions. The dielectrics are mapped by creating mesh subdomains with different dielectric constants within the overall domain of the cavity.

After the mesh has been created, we instantiate portable extensible toolkit for scientific computation (PETSc) matrices, assemble the matrices with the equations from the weak form, and then apply the two Dirichlet boundary conditions. The first boundary condition forces $\mathbf{E} = 0$ on the conductive boundary, while the second boundary condition forces $E_\phi = 0$ on the central axis, both of which are required for the quasi TE_{011} mode. (Other TE and TM modes will be found, which also satisfy those two boundary conditions.) The program then solves for λ and $\mathbf{e}$ with a scalable library for eigenvalue problem computation (SLEPc) eigensolver, around some target frequency provided. If a resonant mode is found, the get_eigenpair function in FEniCS returns four objects which are the real and complex solutions of the electric field and the resonant frequency. Since the resonant modes of the cylindrical cavity have real electric fields and resonant frequencies, the complex solutions are ignored while the real solutions undergo further testing to determine whether they characterize the quasi TE_{011} mode as described in the body of this article.

ACKNOWLEDGMENT

The authors gratefully acknowledge K. Miller for some valuable preliminary discussions, including the derivation of (3).

REFERENCES

[1] J. A. Weil and J. R. Bolton, "Appendix E: Instrumentation and technical performance," in *Electron Paramagnetic Resonance: Elementary Theory and Practical Applications*, 2nd ed. Hoboken, NJ, USA: Wiley, 2007, pp. 512-536.

[2] J. S. Colton and L. R. Wienkes, "Resonant microwave cavity for 8.5–12 GHz optically detected electron spin resonance with simultaneous nuclear magnetic resonance," *Rev. Sci. Instrum.*, vol. 80, no. 3, Mar. 2009, Art. no. 035106.

[3] A. G. Webb, "Dielectric materials in magnetic resonance," *Concepts Magn. Reson. A*, vol. 38A, no. 4, pp. 148–184, Jul. 2011.

[4] A. Blank, E. Suhovoy, R. Halevy, L. Shtirberg, and W. Harneit, "ESR imaging in solid phase down to sub-micron resolution: Methodology and applications," *Phys. Chem. Chem. Phys.*, vol. 11, pp. 6689–6699, Jul. 2009.

[5] J. Beckers *et al.*, "Mapping electron dynamics in highly transient EUV photon-induced plasmas: A novel diagnostic approach using multi-mode microwave cavity resonance spectroscopy," *J. Phys. D, Appl. Phys.*, vol. 52, no. 3, Jan. 2019, Art. no. 034004.

[6] D. E. Nagle, E. A. Knapp, and B. C. Knapp, "Coupled resonator model for standing wave accelerator tanks," *Rev. Sci. Instrum.*, vol. 38, no. 11, pp. 1583–1587, Nov. 1967.

[7] C. Gao, E. Li, Y. Zhang, Y. Gao, and L. Huang, "Permittivity measurement of the dielectric material at the off-axis position in a cylindrical cavity," *IEEE Trans. Microw. Theory Techn.*, vol. 69, no. 3, pp. 1711–1722, Mar. 2021.

[8] C. N. Works, "Resonant cavities for dielectric measurements," *J. Appl. Phys.*, vol. 18, no. 7, pp. 605–612, Jul. 1947.

[9] S. B. Cohn, "Microwave bandpass filters containing high-Q dielectric resonators," *IEEE Trans. Microw. Theory Techn.*, vol. MTT-16, no. 4, pp. 218–227, Apr. 1968.

[10] S. J. Fiedziuszko, "Dual-mode dielectric resonator loaded cavity filters," *IEEE Trans. Microw. Theory Techn.*, vol. MTT-30, no. 9, pp. 1311–1316, Sep. 1982.

[11] A. Okaya and L. F. Barash, "The dielectric microwave resonator," *Proc. IRE*, vol. 50, no. 10, pp. 2081–2092, Oct. 1962.

[12] S. Long, M. McAllister, and L. C. Shen, "The resonant cylindrical dielectric cavity antenna," *IEEE Trans. Antennas Propag.*, vol. AP-31, no. 3, pp. 406–412, May 1983.

[13] C. Weickhmann, "Liquid crystals towards terahertz: Characterisation and tunable waveguide phase shifters for millimetre-wave and terahertz beamsteering antennas," Ph.D. dissertation, Dept. Elektrotechnik Informationstechnik, Technischen Univ. Darmstadt, Darmstadt, Germany, 2017.

[14] S. Keyrouz and D. Caratelli, "Dielectric resonator antennas: Basic concepts, design guidelines, and recent developments at millimeter-wave frequencies," *Int. J. Antennas Propag.*, vol. 2016, Oct. 2016, Art. no. 6075680.

[15] A. Khalajmehrabadi, M. K. A. Rahim, and M. Khalily, "Dual band double stacked dielectric resonator antenna with a P-shape parasitic strip for circular polarization," in *Proc. IEEE Int. RF Microw. Conf. (RFM)*, Dec. 2011, pp. 444–447.

[16] R. S. Alger, *Electron Paramagnetic Resonance: Techniques and Applications*. New York, NY, USA: Interscience, 1968, p. 127.

[17] R. D. Richtmyer, "Dielectric resonators," *J. Appl. Phys.*, vol. 10, no. 6, pp. 391–398, Jun. 1939.

[18] D. L. Carter and A. Okaya, "Electron paramagnetic resonance of Fe^{3+} in TiO_2 (rutile)," *Phys. Rev.*, vol. 118, no. 6, pp. 1485–1490, Jun. 1960.

[19] F. J. Rosenbaum, "Dielectric cavity resonator for ESR experiments," *Rev. Sci. Instrum.*, vol. 35, no. 11, pp. 1550–1554, Nov. 1964.

[20] W. M. Walsh and L. W. Rupp, "Enhanced ESR sensitivity using a dielectric resonator," *Rev. Sci. Instrum.*, vol. 57, no. 9, pp. 2278–2279, Sep. 1986.

[21] R. W. Dykstra and G. D. Markham, "A dielectric sample resonator design for enhanced sensitivity of EPR spectroscopy," *J. Magn. Reson.*, vol. 69, no. 2, pp. 350–355, Sep. 1986.

[22] G. Annino, M. Cassettari, I. Longo, and M. Martinelli, "Dielectric resonators in ESR: Overview, comments and perspectives," *Appl. Magn. Reson.*, vol. 16, no. 1, pp. 45–62, Jan. 1999.

[23] A. Blank, E. Stavitski, H. Levanon, and F. Gubaydullin, "Transparent miniature dielectric resonator for electron paramagnetic resonance experiments," *Rev. Sci. Instrum.*, vol. 74, no. 5, pp. 2853–2859, May 2003.

[24] I. Golovina, I. Geifman, and A. Belous, "New ceramic EPR resonators with high dielectric permittivity," *J. Magn. Reson.*, vol. 195, no. 1, pp. 52–59, Nov. 2008.

[25] S. Friedländer, O. Ovchar, H. Voigt, R. Böttcher, A. Belous, and A. Pöppl, "Dielectric ceramic EPR resonators for low temperature spectroscopy at X-band frequencies," *Appl. Magn. Reson.*, vol. 46, no. 1, pp. 33–48, Jan. 2015.

[26] S. Friedländer *et al.*, "Single crystal electron paramagnetic resonance with dielectric resonators of mononuclear Cu^{2+} ions in a metal–organic framework containing Cu_2 paddle wheel units," *J. Phys. Chem. C*, vol. 119, no. 33, pp. 19171–19179, Aug. 2015.

[27] M. Schreiner, H. Pascher, G. Denninger, S. A. Studenikin, G. Weimann, and R. Lösch, "Nuclear spin relaxation in AlGAas/GaAs heterostructures observed via optically detected magnetic resonance (ODMR) experiments," *Solid State Commun.*, vol. 102, pp. 715–720, Jun. 1997.

[28] S. E. Bromberg and I. Y. Chan, "Enhanced sensitivity for high-pressure EPR using dielectric resonators," *Rev. Sci. Instrum.*, vol. 63, no. 7, pp. 3670–3673, Jul. 1992.

[29] T. Kambe, M. Fujiwara, K. Oshima, S. Garaj, A. Sienkiewisz, and L. Forró, "High pressure ESR system with double-stacked dielectric resonators-its application to the polymerization of the TDAE-C_{60} organic ferromagnet," *J. Phys. Soc. Jpn.*, vol. 72, pp. 151–155, Jan. 2003.

[30] A. Sienkiewicz, B. Vileno, S. Garaj, M. Jaworski, and L. Forró, "Dielectric resonator-based resonant structure for sensitive ESR measurements at high-hydrostatic pressures," *J. Magn. Reson.*, vol. 177, no. 2, pp. 261–273, Dec. 2005.

[31] T. Neuberger *et al.*, "Design of a ceramic dielectric resonator for NMR microimaging at 14.1 Tesla," *Concepts Magn. Reson. B, Magn. Reson. Eng.*, vol. 33B, no. 2, pp. 109–114, Apr. 2008.

[32] S. J. Fiedziuszko, "Oscillator applications of double dielectric resonator," in *IEEE MTT-S Int. Microw. Symp. Dig.*, vol. 2, May 1988, pp. 613–616.

[33] G. Lassmann, P. P. Schmidt, and W. Lubitz, "An advanced EPR stopped-flow apparatus based on a dielectric ring resonator," *J. Magn. Reson.*, vol. 172, no. 2, pp. 312–323, Feb. 2005.

[34] S. M. Mattar and S. Y. El Naggar, "Analysis of two stacked cylindrical dielectric resonators in a TE_{102} microwave cavity for magnetic resonance spectroscopy," *J. Magn. Reson.*, vol. 209, no. 2, pp. 174–182, Apr. 2011.

[35] T. Yasukawa, A. J. Sigillito, B. C. Rose, A. M. Tyryshkin, and S. A. Lyon, "Addressing spin transitions on ^{209}Bi donors in silicon using circularly polarized microwaves," *Phys. Rev. B, Condens. Matter*, vol. 93, no. 12, Mar. 2016, Art. no. 121306(R).

[36] S. M. Mattar and S. Y. Elnaggar, "Modes and fields of two stacked dielectric resonators in a cavity of an electron paramagnetic resonance probe," *Appl. Magn. Reson.*, vol. 48, nos. 11–12, pp. 1205–1217, Dec. 2017.

[37] A. Sienkiewicz, K. Qu, and C. P. Scholes, "Dielectric resonator-based stopped-flow electron paramagnetic resonance," *Rev. Sci. Instrum.*, vol. 65, no. 1, pp. 68–74, Jan. 1994.

[38] E. Stavitski, L. Wagnert, and H. Levanon, "Magnetic field dependence of electron spin polarization generated through radical-triplet interactions," *J. Phys. Chem. A*, vol. 109, no. 6, pp. 976–980, Jan. 2005.

[39] H. Y. Yee, "Natural resonant frequencies of microwave dielectric resonators (correspondence)," *IEEE Trans. Microw. Theory Techn.*, vol. MTT-13, no. 2, p. 256, Mar. 1965.

[40] S. Fiedziuszko and A. Jalenski, "Double dielectric resonator (correspondence)," *IEEE Trans. Microw. Theory Techn.*, vol. MTT-19, no. 9, pp. 779–781, Sep. 1971.

[41] S. Fiedziuszko and A. Jelenski, "The influence of conducting walls on resonant frequencies of the dielectric microwave resonator (correspondence)," *IEEE Trans. Microw. Theory Techn.*, vol. MTT-19, no. 9, pp. 778–779, Sep. 1971.

[42] T. Itoh and R. S. Rudokas, "New method for computing the resonant frequencies of dielectric resonators (short papers)," *IEEE Trans. Microw. Theory Techn.*, vol. MTT-25, no. 1, pp. 52–54, Jan. 1977.

[43] M. W. Pospieszalski, "Cylindrical dielectric resonators and their applications in TEM line microwave circuits," *IEEE Trans. Microw. Theory Techn.*, vol. MTT-27, no. 3, pp. 233–238, Mar. 1979.

[44] M. Jaworski, A. Sienkiewicz, and C. P. Scholes, "Double-stacked dielectric resonator for sensitive EPR measurements," *J. Magn. Reson.*, vol. 124, no. 1, pp. 87–96, Jan. 1997.

[45] Y. Konishi, N. Hoshino, and Y. Utsumi, "Resonant frequency of a $TE_{01\delta^\circ}$ dielectric resonator," *IEEE Trans. Microw. Theory Techn.*, vol. MTT-24, no. 2, pp. 112–114, Feb. 1976.

[46] A. W. Glisson, D. Kajfez, and J. James, "Evaluation of modes in dielectric resonators using a surface integral equation formulation," *IEEE Trans. Microw. Theory Techn.*, vol. MTT-31, no. 12, pp. 1023–1029, Dec. 1983.

[47] D. Kajfez, A. W. Glisson, and J. James, "Computed modal field distributions for isolated dielectric resonators," *IEEE Trans. Microw. Theory Techn.*, vol. MTT-32, no. 12, pp. 1609–1616, Dec. 1984.

[48] R. K. Mongia and B. Bhat, "Accurate resonant frequencies of cylindrical dielectric resonators using a simple analytical technique," *Electron. Lett.*, vol. 21, no. 11, pp. 479–480, May 1985.

[49] J. Lee and Y.-S. Kim, "A new method of accurately determining resonant frequencies of cylindrical and ring dielectric resonators," *IEEE Trans. Microw. Theory Techn.*, vol. 47, no. 6, pp. 706–708, Jun. 1999.

[50] K. G. Miller, M. Meehan, R. L. Spencer, and J. S. Colton, "Resonance of complex cylindrically symmetric cavities using an eigenfunction expansion in empty cavity modes," *IEEE Trans. Microw. Theory Techn.*, vol. 64, no. 10, pp. 3113–3120, Oct. 2016.

[51] S. Y. Elnaggar, R. Tervo, and S. M. Mattar, "General expressions for the coupling coefficient, quality and filling factors for a cavity with an insert using energy coupled mode theory," *J. Magn. Reson.*, vol. 242, pp. 57–66, May 2014.

[52] R. Ghosal, S. Maity, B. Gupta, and A. Majumder, "Analytical prediction of resonant frequencies of annular stacked dielectric resonator antennas," *Int. J. RF Microw. Comput.-Aided Eng.*, vol. 30, no. 8, Apr. 2020, Art. no. e22237.
[53] P. Guillon, J. P. Balabaud, and Y. Garault, "TM01p tubular and cylindrical dielectric resonator mode," in *IEEE MTT-S Int. Microw. Symp. Dig.*, Jun. 1981, pp. 163–166.
[54] J. E. Lebaric and D. Kajfez, "Analysis of dielectric resonator cavities using the finite integration technique," *IEEE Trans. Microw. Theory Techn.*, vol. 37, no. 11, pp. 1740–1748, Nov. 1989.
[55] M. Wiktor and M. Mrozowski, "Fast numerical analysis of dielectric resonators with perturbed rotational symmetry," *IEEE Microw. Wireless Compon. Lett.*, vol. 15, no. 8, pp. 516–518, Aug. 2005.
[56] D. Baillargear, S. Verdeyme, M. Aubourg, and P. Guillon, "CAD applying the finite-element method for dielectric-resonator filters," *IEEE Trans. Microw. Theory Techn.*, vol. 46, no. 1, pp. 10–17, Jan. 1998.
[57] R. Dyczij-Edlinger, G. Peng, and J.-F. Lee, "Efficient finite element solvers for the Maxwell equations in the frequency domain," *Comput. Methods Appl. Mech. Eng.*, vol. 169, nos. 3–4, pp. 297–309, Feb. 1999.
[58] W. Jiang, N. Liu, Y. Yue, and Q. H. Liu, "Mixed finite-element method for resonant cavity problem with complex geometric topology and anisotropic lossless media," *IEEE Trans. Magn.*, vol. 52, no. 2, Feb. 2016, Art. no. 7400108.
[59] Z. Guan, J. Liu, M. Zhuang, and Q. H. Liu, "A hybrid SESI method for electromagnetic scattering by objects in multiregion cylindrically layered media," *IEEE Trans. Microw. Theory Techn.*, vol. 69, no. 9, pp. 3967–3975, Sep. 2021.
[60] H. P. Langtangen and A. Logg, *Solving PDEs in Python—The FEniCS Tutorial*, vol. 1. Springer, 2017, pp. 3–37. [Online]. Available: https://link.springer.com/book/10.1007/978-3-319-52462-7#about
[61] J. D. Jackson, *Classical Electrodynamics*, 3rd ed. Hoboken, NJ, USA: Wiley, 1999, pp. 352–406.
[62] J. F. Swidzinski and K. Chang, "Nonlinear statistical modeling and yield estimation technique for use in Monte Carlo simulations," *IEEE Trans. Microw. Theory Techn.*, vol. 48, no. 12, pp. 2316–2324, Dec. 2000.
[63] M. D. McKay, R. J. Beckman, and W. J. Conover, "A comparison of three methods for selecting values of input variables in the analysis of output from a computer code," *Technometrics*, vol. 21, no. 2, pp. 239–245, May 1979.
[64] J. S. Hyde and R. R. Mett, "EPR uniform field signal enhancement by dielectric tubes in cavities," *Appl. Magn. Reson.*, vol. 48, nos. 11–12, pp. 1185–1204, Sep. 2017.
[65] N. Warwar, A. Mor, R. Fluhr, R. P. Pandian, P. Kuppusamy, and A. Blank, "Detection and imaging of superoxide in roots by an electron spin resonance spin-probe method," *Biophys. J.*, vol. 101, no. 6, pp. 1529–1538, Sep. 2011.
[66] L. Shtirberg, Y. Twig, E. Dikarov, R. Halevy, M. Levit, and A. Blank, "High-sensitivity Q-band electron spin resonance imaging system with submicron resolution," *Rev. Sci. Instrum.*, vol. 82, no. 4, Apr. 2011, Art. no. 043708.
[67] A. G. Webb, "Visualization and characterization of pure and coupled modes in water-based dielectric resonators on a human 7T scanner," *J. Magn. Reson.*, vol. 216, pp. 107–113, Mar. 2012.
[68] G. Pelosi, R. Cocciolo, and S. Selleri, *Quick Finite Elements for Electromagnetic Waves*, 2nd ed. Boston, MA, USA: Artech House, 2009, pp. 191–208.
[69] A. Logg *et al.*, *Automated Solution of Differential Equations by the Finite Element Method*, A. Logg, K. Mardal, and G. N. Wells, Eds. Springer, 2012, pp. 629–642. [Online]. Available: https://fenicsproject.org/book/

Charles Lewis (Graduate Student Member, IEEE) received the B.S. degree in physics from Brigham Young University, Provo, UT, USA, in 2020. He is currently pursuing the Ph.D. degree in physics at the University of Washington, Seattle, WA, USA.

He participated in a research semester in 2018 at the European Organization for Nuclear Research (CERN) with the University of Michigan, Ann Arbor, MI, USA, working on the ATLAS experiment. In 2019, he was a DAAD-RISE Intern with the Juelich Forschungszentrum's Nuclear Physics Institute (IKP), Juelich, Germany.

Jordan Bryan received the B.S. degree in physics and computational physics from Illinois State University (ISU), Normal, IL, USA, in 2021.

In 2020, she completed a research experience for undergraduates with Brigham Young University, Provo, UT, USA. She is currently working as a Research Partner with ISU while pursuing a career in data science.

Nathan Schwartz received the B.S. degree (*magna cum laude*) in applied physics from Brigham Young University, Provo, UT, USA, in 2021.

He currently works as a Consultant with Oliver Wyman, Dallas, TX, USA, where he advises primarily in the healthcare and technology industries.

Mr. Schwartz received an award for his presentation on condensed matter physics at the Annual BYU Student Research Conference.

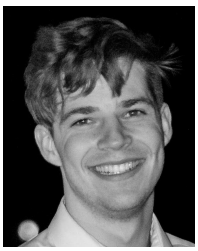

Jonathan Hale received the B.S. degree in applied mathematics from Brigham Young University (BYU), Provo, UT, USA, in 2021, where he is currently pursuing the M.S. degree in mathematics.

He is planning to pursue a graduate degree in medical physics after his time at BYU. His research interests include smooth grid generation for use in numerical methods for partial differential equations (PDEs).

Kane Fanning is currently pursuing the B.S. degree in physics and mathematics at Brigham Young University, Provo, UT, USA.

His research interest currently includes developing computational methods for studying magnetic materials on small scales.

John S. Colton received the B.S. degree in physics and mathematics from Brigham Young University (BYU), Provo, UT, USA, in 1994, and the M.S. degree in physics and the Ph.D. degree in condensed matter physics from the University of California at Berkeley, Berkeley, CA, USA, in 1997 and 2000, respectively.

He was a Post-Doctoral Researcher with the U.S. Naval Research Laboratory, Washington, DC, USA, from 2000 to 2003. He was an Assistant Professor with the University of Wisconsin–La Crosse, La Crosse, WI, USA, from 2003 to 2007. He is currently an Associate Professor with BYU. His current research interest includes the optical spectroscopy of semiconductors with an emphasis on spin properties and semiconductor nanostructures.

Dr. Colton is a member of the American Physical Society and the American Association of Physics Teachers.